



Tropospheric ozone sensing with a differential absorption lidar based on a single CO₂ Raman cell

Guangqiang Fan¹, Yibin Fu¹, Juntao Huo³, Yan Xiang⁴, Tianshu Zhang^{1,2}, Wenqing Liu¹, and Zhi Ning⁵

¹Key Laboratory of Environmental Optics and Technology, Anhui Institute of Optics and Fine Mechanics, Chinese Academy of Sciences, Hefei, 230031, China

²Institute of Environment, Hefei Comprehensive National Science Center, Hefei 230088, China

³Shanghai Environmental Monitoring Center, Shanghai, 200235, China

⁴Information Materials and Intelligent Sensing Laboratory of Anhui Province, Institute of Physical Science and Information Technology, Anhui University, Hefei 230601, China

⁵Division of Environment and Sustainability, The Hong Kong University of Science and Technology, Hong Kong SAR, China

Correspondence: Yan Xiang (yxiang@ahu.edu.cn) and Tianshu Zhang (tszhang@aiofm.ac.cn)

Received: 25 June 2024 – Discussion started: 10 July 2024

Revised: 18 October 2024 – Accepted: 19 November 2024 – Published: 27 January 2025

Abstract. This study presents the development and performance evaluation of an ozone differential absorption lidar system. The system could effectively obtain vertical profiles of lower-tropospheric ozone in an altitude range of 0.3 to 4 km with high spatiotemporal resolutions. The system emits three laser beams at wavelengths of 276, 287 and 299 nm by using the stimulated Raman effect of carbon dioxide (CO₂). A 250 mm telescope and a grating spectrometer are used to collect and separate the backscattering signals at the three wavelengths. Considering the influences of aerosol interference and statistical error, a wavelength pair of 276–287 nm is used for the altitude below 600 m and a wavelength pair of 287–299 nm is used for the altitude above 600 m to invert ozone concentration. We also evaluated the errors caused by the uncertainty of the wavelength index. The developed ozone lidar was deployed in a field campaign that was conducted to measure the vertical profiles of ozone using a tethered balloon platform. The lidar observations agree very well with those of the tethered balloon platform.

important air pollutant that impacts the oxidative capacity of the atmosphere (Wang et al., 2017). It is highly reactive with the oxidative potential to damage biological tissue and adversely impact human health, vegetation, crop yield and crop quality. As a result of ozone's high reactivity, the lifetime of ozone in the lower troposphere is short with significant differences in spatial and temporal distributions. For a specific region, tropospheric ozone mainly originates from the photochemical production of local anthropogenic and biogenic emissions (Koo et al., 2012; Chi et al., 2018), regionally advection transport (Schuepbach et al., 1999; Wang et al., 2021), and stratosphere–troposphere exchange (Clain et al., 2010; Olsen et al., 2004; Wang et al., 2023). With such dynamic sources, it is essential to monitor both vertical and temporal distributions of tropospheric ozone for making effective control strategies of ozone pollution.

At the surface, in situ ultraviolet analyzers can measure ozone concentrations with high temporal resolutions and a high accuracy of within 5% (Sullivan et al., 2014). A national network of surface ozone monitoring has been gradually established covering nearly all the cities in China over the past few decades. The measurements of these surface stations are typically in 8 h averaged or hourly averaged values, which are effective for analyzing surface ozone trends. However, it is essential to analyze vertical variations in lower-tropospheric ozone when dramatic changes of surface ozone occur. There are several useful methods, including tethered

1 Introduction

Tropospheric ozone is an important greenhouse gas and plays an important role in the Earth's radiation budget with an estimated direct radiative forcing of 0.4 W m⁻² during the industrial era (Chen et al., 2020). At the surface, ozone is an

balloon (Li et al., 2018), sounding balloon (Lokoshchenko et al., 2009) and aircraft (Langford et al., 2019), that have been successfully used to obtain vertical profiles of lower-tropospheric ozone. However, the measurements made by these methods have limited spatial and temporal variations and cannot fully characterize the distribution and evolution patterns of ozone in the lower troposphere. Ozone profiles from the Tropospheric Emission Spectrometer and the Ozone Mapping Instrument have been reported (Osterman et al., 2008; Worden et al., 2007; Qian et al., 2021), while the vertical resolution for tropospheric ozone is strictly limited.

The continuous vertical and temporal distributions of ozone in the troposphere can be detected by differential absorption lidars with much higher frequency and accuracy. Dating back to the 1970s, this technique was first used to monitor water vapor. The technique was then successfully modified and utilized for accurate ozone detection. For ozone detection, the differential absorption lidars can be divided into two groups according to the types of laser technology: tunable-laser technology and fixed-frequency conversion technology. The advantage of tunable laser technology for ozone detection relies on its optimal detection wavelengths, which contributes to optimal detection sensitivity improvements including small aerosol and other gas interference. The second harmonic of Nd:YAG lasers pumps the dye laser and produces a series of waves in the range of 272–310 nm via the double-frequency crystal as the light source of ozone detection. Most ozone lidars use two separate dye lasers to generate both on and off wavelength pairs at the same time (Kuang et al., 2013). The differential absorption lidar based on this technique usually has a complex system and requires a wavelength stabilization feedback device to monitor and control the laser wavelength in real time. In addition, dye lasers need to be replaced frequently due to a limited lifetime of the dyes, some of which contain carcinogens and are harmful for the operators' health. Given these drawbacks, for the purpose of optimizing ozone detection, researchers have developed a pulsed optical parametric oscillator with intracavity sum frequency mixing, generating lasers in the wavelength range of 281–293 nm (Fix et al., 2002).

Moreover, excimer lasers or Nd:YAG lasers are also used in some studies as the pumping lasers. H₂ and D₂ Raman gases are pumped to produce Stokes lights for ozone detection (Hwang et al., 1993; Fan et al., 2024). The National Oceanic and Atmospheric Administration (NOAA) deployed a scanning four-wavelength ultraviolet differential absorption lidar (Machol et al., 2009). The lidar system measures tropospheric ozone and aerosols by utilizing the Raman shift wavelengths generated from D₂ and H₂ gases. However, there are two primary challenges associated with employing the D₂ and H₂ dual Raman cells: (1) shared laser resource – the D₂ and H₂ Raman cells are both pumped by the same frequency-quadrupled Nd:YAG laser. This shared resource places increased demands on the pump laser's performance and stability. The laser must provide sufficient energy to ef-

fectively pump both Raman cells. (2) The second is receiver field of view and laser divergence overlap – this challenge arises from the varying overlaps between the receiver's field of view and the divergences of the laser beams for the D₂ and H₂ Raman cells. These differences can result in a larger blind area during ozone detection. The blind area refers to the region where the lidar system is unable to accurately measure ozone concentrations due to the geometric constraints of the laser beam and the receiver's field of view. This can lead to incomplete or inaccurate data regarding the ozone levels in the troposphere. In contrast, an ozone lidar system utilizing a CO₂ single Raman cell has the potential to address these issues. The single Raman cell design simplifies the system by eliminating the need to manage two separate Raman cells, thereby reducing complexity and the need for Nd:YAG. Furthermore, the single Raman cell system may offer a more consistent overlap between the receiver's field of view and the laser beam, which can help to minimize the blind area and enhance the accuracy of ozone detection.

However, until now, only a few studies developed the ozone lidar using a single CO₂ Raman cell to detect ozone in both the planetary boundary layer and the free troposphere simultaneously. Many uncertainties including aerosol-interference-induced errors and the system errors caused by wavelength index uncertainty are worth a more thorough investigation conducted by researchers.

In this paper, we present an ozone differential absorption lidar system based on the single CO₂ Raman cell and the grating spectrometer. The wavelength selection and theoretical analysis of aerosol interference errors are discussed in Sect. 2. The design and architecture of the ozone lidar are introduced in detail in Sect. 3. An analysis of statistical errors and the system errors caused by Angstrom wavelength index uncertainty is discussed in Sects. 4 and 5, respectively. Finally, the Sect. 6 provides a typical field validation for the ozone lidar developed in this study by using ozone vertical observations of a tethered balloon platform.

2 Theoretical analysis

According to the dual-wavelength differential absorption algorithm, the ozone concentration $N(z)$ can be expressed as follows (Dolgii et al., 2017).

$$N(z) = \frac{1}{2\Delta\delta} \frac{d}{dz} \left[-\ln \left(\frac{P(\lambda_{\text{on}}, z)}{P(\lambda_{\text{off}}, z)} \right) \right] + B - E_a - E_m - E_{\text{gas}} \quad (1)$$

$$B = \frac{1}{2\Delta\delta} \frac{d}{dz} \left[\ln \left(\frac{\beta(\lambda_{\text{on}}, z)}{\beta(\lambda_{\text{off}}, z)} \right) \right] \quad (2)$$

$$E_a = \frac{1}{\Delta\delta} [\alpha_a(\lambda_{on}, z) - \alpha_a(\lambda_{off}, z)] \quad (4)$$

$$E_m = \frac{1}{\Delta\delta} [\alpha_m(\lambda_{on}, z) - \alpha_m(\lambda_{off}, z)] \quad (5)$$

$$E_{gas} = \frac{\Delta\delta_{gas} N'_{gas}}{\Delta\delta} \quad (6)$$

Here $P(\lambda_i, z)$ is the atmospheric backscatter echo signal at wavelength λ_i and range z ; i is on or off; $\Delta\delta = \delta_{\lambda_{on}} - \delta_{\lambda_{off}}$ is the differential absorption cross section of ozone; B , E_a and E_m are the systematic errors from atmospheric backscattering, aerosol extinction and molecular extinction; E_{gas} is the systematic error introduced by the absorption effect of other trace gasses; $\beta(\lambda_i, z)$ is total atmospheric volume backscatter coefficient at wavelength λ_i and range z ; $\alpha(\lambda_i, z)$ is total atmospheric optical extinction coefficient neglecting ozone absorption at wavelength λ_i and range z ; $\Delta\delta_{gas}$ is the differential absorption cross section of other trace gases; N'_{gas} is the concentration of other trace gases; and α_a and α_m are the extinction coefficients of atmospheric particulate matter and molecular, respectively.

The distribution of molecules in the atmosphere is stable, exhibiting less variability. Therefore, the atmospheric molecular extinction coefficient is directly used to correct E_m . Generally, B and E_a cannot be neglected in the measurements of boundary layer ozone when using the differential absorption method due to the atmospheric backscattering and aerosol extinction coefficients exhibiting strong wavelength dependence. Given that $\Delta\lambda = \lambda_{off} - \lambda_{on}$ is small, the aerosol extinction correction E_a and the backscatter correction B can be estimated using the following equations (Nakazato et al., 2007).

$$E_a \approx -\frac{\Delta\lambda}{\Delta\delta\lambda_{off}} k\alpha_a(\lambda_{off}, z) \quad (7)$$

$$B \approx \frac{(4-\mu)}{2dz\Delta\delta} \cdot \frac{\Delta\lambda}{\lambda_{off}} \cdot \left[\frac{S_{off}(r)}{1+S_{off}(r)} - \frac{S_{off}(r+dz)}{1+S_{off}(r+dz)} \right] \quad (8)$$

$$SF = \frac{1}{\frac{\Delta\delta}{\Delta\lambda}\lambda_{off}} \quad (9)$$

Here k and μ are the power-law exponents for backscattering and extinction, $S_{off}(r)$ is the aerosol backscatter ratio, and SF is referred to as the spectrum factor or the differential aerosol backscatter sensitivity. E_a and B are proportional to SF. E_a is proportional to k , and B is proportional to $(4-\mu)$. As reported in previous studies, the Angstrom wavelength index was generally in the range of 0.6 to 1.4 and exhibited strong spatial and temporal variations. Therefore, it is assumed that the values of k and μ vary in this range. However, the values of k and μ were assumed to be 1 when calculating aerosol correction terms using measured data. Due to the changes in k and μ , E_a had an error of 40%; the B error is within 13%. The aerosol interference is inevitable if the values of k and

Table 1. SF of the differential absorption wavelength pairs.

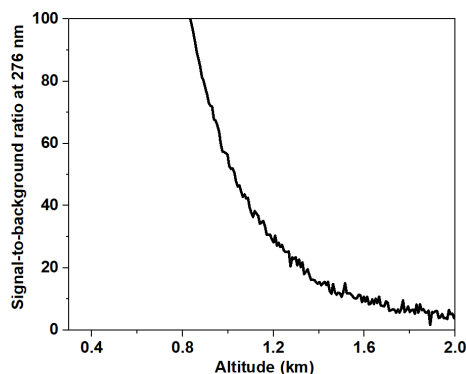
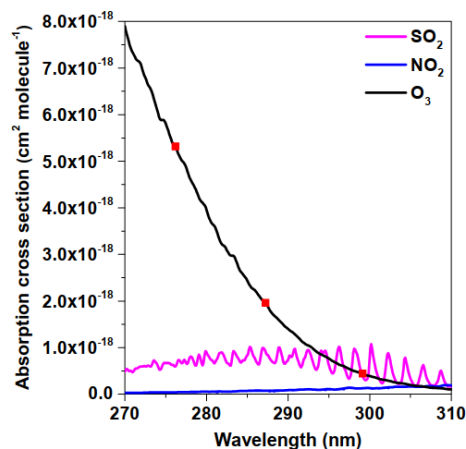
Wavelength pairs (nm)	$\Delta\delta$ (10^{-20} cm ²)	$\Delta\lambda$ (nm)	SF (10^{-16} cm ²)
289/316.4	152.61	27.4	5.67
299.1/316.4	39.79	17.3	13.74
289/299.1	112.82	10.1	3.01
266/289	773.4	23	1.03
276.2/287.2	335.43	11	1.14
287.2/299.1	152.21	11.9	2.61

μ are uncertain, which makes it crucial for the choice of SF. Theoretically, the smaller the SF is, the smaller the influence of aerosol interference on ozone retrieval results is.

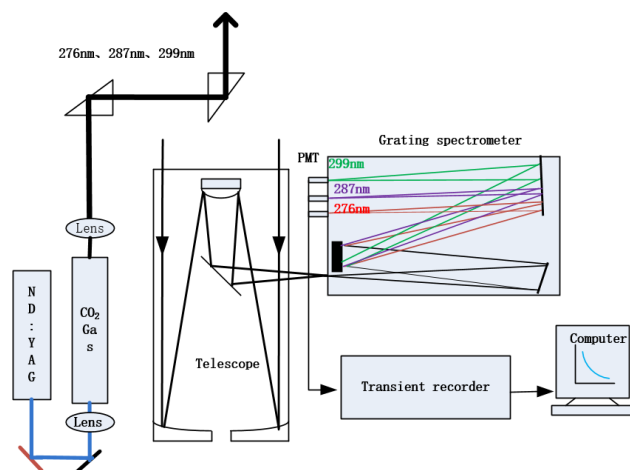
The Nd:YAG quad-frequency laser, when used to pump a single D₂ Raman tube, generates both first-order and second-order Stokes light. These correspond to the differential absorption wavelengths of 289 and 316 nm, respectively. The pumped D₂ Raman tube and H₂ Raman tube produce first-order Stokes light, corresponding to the differential absorption wavelengths of 289 nm and 299 nm, respectively. 289 nm and 316 nm, 289 nm and 299 nm, and 266 nm and 289 nm are common differential absorption wavelength pairs for ozone retrieval. An Nd:YAG quad-frequency pump laser is used to excite a single CO₂ Raman tube, which generates first-order, second-order and third-order Stokes light at corresponding differential absorption wavelengths of 276.2, 287.2 and 299.1 nm, respectively. Table 1 lists the SF of the differential absorption wavelength pairs. The SF of the differential absorption wavelength pair of 276.2 and 287.2 nm is nearly half of that of the 287.2 and 299.1 nm pair, indicating that E_a and B of the wavelength pair of 276.2 and 287.2 nm are nearly half of that of the wavelength pair of 287.2 and 299.1 nm. Due to the strong absorption of ozone at 276 nm and the strong atmospheric backscatter at this wavelength, the detection height of the 276 nm wavelength signal is limited. As shown in Fig. 1, the signal-to-background ratio of the 276 nm signal is greater than 100 below 600 m, which meets the detection requirements with a sufficient signal-to-noise ratio. Above 800 m, it quickly drops below 100. To accommodate different aerosol types and weather influences, and considering that aerosols are mainly distributed below a height of 600 m, a height of 600 m was adopted as the stitching height for the differential wavelength pair. Above 600 m, we adopted the wavelength pairs of 287.2 and 299.1 nm for ozone detection. The SF of the wavelength pair of 287.2 nm and 299.1 nm is slightly smaller than the wavelength pair of 289 nm and 299.1 nm, which is the most widely used wavelength pair in gas Raman tube technology, indicating that E_a and B of 287.2 and 299.1 nm are smaller. The SF of the wavelength pair of 287.2 nm and 299.1 nm is half that of the wavelength pair of 289 and 316.4 nm, so the aerosol interference term is half that of the wavelength pair of 289 and 316.4 nm.

Table 2. The interference of NO₂ and SO₂.

Wavelength pairs (nm)	SO ₂ (e ⁻²⁰ cm ²)	NO ₂ (e ⁻²⁰ cm ²)	O ₃ (e ⁻²⁰ cm ²)	NO ₂ interference	SO ₂ interference
276.2 and 287.2	30	3.3	335.43	0.98 % of the NO ₂ concentration	8.9 % of the SO ₂ concentration
287.2 and 299.1	52.8	5.4	152.21	3.5 % of the NO ₂ concentration	34.7 % of the SO ₂ concentration

**Figure 1.** The signal-to-background ratio at 276 nm wavelength.**Figure 2.** The absorption cross sections of O₃, NO₂ and SO₂ at 276.2, 287.2 and 299.1 nm.

According to Eq. (5), the influence of NO₂ and SO₂ on the O₃ retrieval can be determined. Figure 2 shows the absorption cross sections of O₃, NO₂ and SO₂ at 276.2, 287.2 and 299.1 nm. Table 1 analyzes the extent of interference from NO₂ and SO₂ gases. The interference from NO₂ at the 276.2 nm and 287.2 nm wavelength pair and the 287.2 nm and 299.1 nm wavelength pair is 0.98 % and 3.5 % of the NO₂ concentration, respectively, which can be neglected. The impact of SO₂ on ozone is more significant, with impacts of 8.9 % and 34.7 % of the SO₂ concentration at the two wavelength pairs. The typical environmental concentra-

**Figure 3.** Schematic diagram of the ozone lidar system based on the single CO₂ Raman cell.

tion of SO₂ is a few micrograms per cubic meter ($\mu\text{g m}^{-3}$). If assessed at $10 \mu\text{g m}^{-3}$, its impact would be approximately 0.89 and $3.5 \mu\text{g m}^{-3}$, which is relatively small compared to other sources of error and is therefore usually not considered.

3 Ozone lidar system architecture

We designed a differential absorption lidar based on a single CO₂ Raman cell for measuring boundary-layer and free-tropospheric ozone. Compared with the D₂ and H₂ Raman tube, this system has a smaller SF to reduce the aerosol interference, which makes it particularly suitable for the detection of lower-tropospheric ozone. Figure 3 shows the schematic diagram of the ozone lidar system developed in this study. The key parameters of the ozone lidar system are listed in Table 2. The ozone lidar is mainly composed of three parts: laser transmitting unit, optical receiving and subsequent optical unit, and data acquisition unit. The whole system is based on the same optical plate with a compact and stable mechanical structure.

Table 3. The key parameters of the differential absorption lidar system.

Cell name	Parameters
Transmitter pumped laser	Nd:YAG (266 nm)
Pulse repetition rate	10 Hz
Pulse energy	90 mJ
Raman-shifted wavelength	276, 287, 299 nm
Output energy	8.4 mJ, 7.7–4.2 mJ
Divergence angle receiver telescope	0.3 mrad Cassegrain
Telescope diameter	250 mm
Detector	Photomultiplier tube
Data acquisition	Analog digitizer
System parameters	
Detection range	0.2–4 km
Temporal resolution	15 min
Spatial resolution	75 m
Statistical error	< 15 % (below 3 km)

3.1 Laser transmitting unit

A flashmap-pumped Nd:YAG laser (Quantel, Q-Smart 850), which provides 90 mJ output at the wavelength of 266 nm and the pulse repetition rate of 10 Hz, is used as the pump source for the CO₂ Raman cell. Considering the volume of the final equipment and the CO₂ stimulated Raman optimization experiment, the Raman cell with a length of 1 m is adopted. The Raman cell is filled with 16 bar (1.6 MPa) pure CO₂ with 99.999 % purity. It has high strength and good tightness. The 266 nm laser is focused near the center of the Raman cell with a 15 mm inner diameter using a 500 mm focal length lens. The Raman cell incident lens and the achromatic lens group constitute a triple beam expansion system, and the laser divergence angle is 0.3 mrad. The energy output of the laser at wavelengths of 276, 287 and 299 is 8.4, 7.7 and 4.2 mJ, respectively. The purpose of adopting an achromatic lens is to minimize the difference of the laser divergence angle at the wavelengths of 276, 287 and 299 nm; to reduce the influence of geometric factors in the lidar transition zone on ozone retrieval; and to increase the lower detection height of the ozone lidar. The arrangement of coaxial transmission and reception was also adopted to further reduce the maximum height of the lidar transition zone.

3.2 Optical receiving and subsequent optical unit

This system deployed a Cassegrain telescope with a diameter of 250 mm and a focal length of 2500 m. The primary and the secondary mirrors of the Cassegrain telescope are hyperboloid mirrors. The telescope is mounted on a rigid optical bench together with the laser transmitting unit. An ultraviolet multiwavelength grating spectrometer is used to separate the echo signals at the wavelengths of 276, 287 and 299 nm. The grating spectrometer includes an aperture, a high-reflection

collimator, a high-resolution holographic grating, three sets of high-reflectivity plano-concave reflectors and three sets of photomultiplier tubes. These components are mounted on an optical plate and sealed by a closed black box to avoid the light interference. The 2 mm aperture is mounted on the focal plane of the receiving telescope, and the received field of view angle of the ozone lidar system is about 0.5 mrad. The echo signals at the wavelengths of 276, 287 and 299 nm are converged by the receiving telescope to form a divergent beam with a numerical aperture of 10. When the signals are transmitted to the grating spectrometer, the lights are collimated by the plano-concave mirror. Through the reflection of the plano-concave mirror, the parallel light arrives at the diffraction grating. The high-resolution planar holographic grating is the core part of the grating spectrometer. Echo signals at the wavelengths of 276, 287 and 299 nm can be separated into different angle positions due to their different diffraction angles. The three sets of high-reflection flat concave mirrors are constructed using JGS1 quartz material, which is chosen for its superior optical properties and resistance to laser damage, ensuring high reflectivity and durability in the system. The plating of high-reflection dielectric film increases the reflectivity to more than 98 % for the optical signals in the ultraviolet band. By adjusting the angles of the three sets of the high-reflection flat concave mirrors, the echo signals could precisely converge on the three sets of photomultiplier tubes. R7400 photomultiplier tubes produced by Hamamatsu are applied, with an effective receiving aperture of 8 mm, short response time and high quantum efficiency in the ultraviolet band of 200–300 nm.

3.3 Data acquisition unit

A 20 M, 12-bit analogue/digital (A/D) data acquisition system is selected to record single-shot raw data, providing a vertical spatial resolution of 7.5 m that is good enough for ozone measurements with vertical resolution ranging from 75 to 200 m. The maximum number of samples is set to 3000 to monitor the sky background noise. Therefore, various background baseline distortions due to the presence of electromagnetic interference or SIN effects in the tail of the lidar signals can be monitored. The echo signals are averaged for as many as 4000 shots (400 s acquisition time) by the software. In order to meet the long-term monitoring requirements and increase the service life of the laser, we stop the flash lamp for 300 s after each echo signal averaging. Thus, the time resolution of the system is 700 s. In order to reduce the influence of the A/D electronic noise on the atmospheric echo signal, amplifiers of 2 times and 48 times are adopted for the same echo signal for the low-altitude signal and the high-altitude signal, respectively. The signal obtained from 15 to 16 km is selected as the background signal, and the standard deviation is calculated as the electronic noise. Taking the echo signal of 287 nm as an example, the influence of different amplifier magnification times on the effective de-

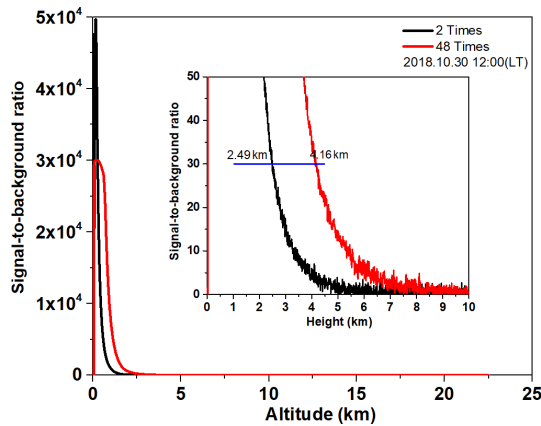


Figure 4. The echo signal at 287 nm wavelength and the signal-to-background ratio.

tection of the signal is illustrated in Fig. 4, with the echo signal at 287 nm and the signal-to-background ratio defined as the ratio of the echo signal to the standard deviation of the background signals. Below 500 m, the signal collected by the acquisition card is saturated with the 48-times amplification of the 280 nm echo signal. The detection heights of the 2-times amplified and 48-times amplified signal are 2.49 and 4.19 km, respectively, when the signal-to-background ratio (SBR) is 30. It can thus be seen that a large magnification can effectively increase the dynamic range of the echo signal as well as improve the detection range of the echo signal. Within the range of 0.5–1 km, the echo signals of the 2-times and 48-times magnification are fused using the least-squares method.

4 Inversion errors analysis

4.1 Analysis of statistical error

The ozone lidar was initially located at the Anhui Institute of Optics and Fine Mechanics in Hefei, China. The experiment was first conducted from 26 October to 3 November 2018, as shown in Fig. 5. Below 600 m, the signals at 276 and 287 nm were used to retrieve the ozone concentration profile; above 600 m, the signals at 287 and 299 nm were used. This image was created by analyzing the measurement results from the 4000 laser pulses emitted to construct a complete profile of the atmosphere from 0.3 to 4 km with a vertical resolution of 100 m. During the observation period, ozone concentrations below 2 km exhibit a distinct diurnal distribution pattern and experienced the processes' gradual accumulation, aggravation and dissipation. High ozone mixing ratios exceeding 60 ppb occurred in most of the afternoon periods from 30 October to 1 November. The statistical error of ozone lidar data is inversely proportional to the absorption cross-section difference, the difference distance, the unknown gas concentra-

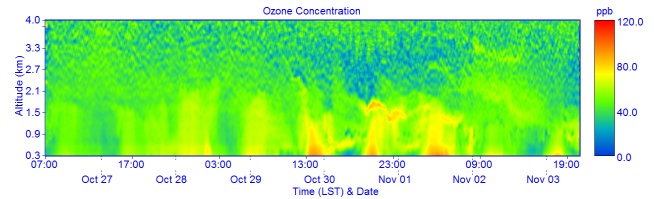


Figure 5. Time series of ozone vertical profiles obtained from the ozone lidar between 26 October and 3 November 2018.

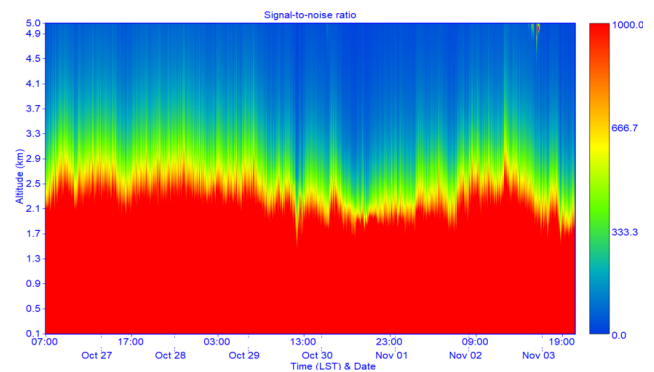


Figure 6. Signal-to-noise ratio of the echo signal at 299.1 nm wavelength.

tion and the signal-to-noise ratio (SNR) of the ozone data. The statistical error of the ozone lidar not only is related to the hardware of the device but can also be considered constant in the short term, aside from its dependence on atmospheric conditions and solar irradiance. Generally, due to the influence of solar irradiance, the SNR of daytime signals is typically lower than that of nighttime signals. During the observation period from 26 October to 3 November 2018, the SNR of the 299.1 nm signal remained essentially stable, as shown in Fig. 6. Therefore, the statistical error of ozone from 11:00 to 12:00 LST (local standard time) on 26 October 2018 was used to analyze the performance of the ozone lidar. It is important to note that an ozone lidar is an in situ measurement device that is closely related to atmospheric conditions and that its SNR can drop sharply during extreme weather conditions such as rain or fog, leading to a significant increase in statistical error. Six profiles measured by the ozone lidar from 11:01 to 12:03 LST on 26 October 2018 were selected for statistical analysis. As shown in Fig. 7, the statistical error in the height range of 200 to 600 m gradually increased from 2.35 % to 6.9 % and it was accompanied by the decrease in the ratio of signal to noise for the echo signals of 276 nm. The statistical error of ozone from 0.6 to 2.7 km was basically within 3 %. From 2.7 to 3.9 km, the statistical error gradually increased to about 18 %, which is due to the gradual deterioration of the signal-to-background ratio with the increase in height.

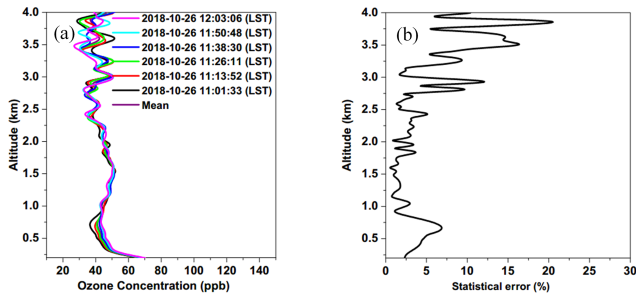


Figure 7. Ozone vertical profile measured by the ozone lidar and its statistical error.

4.2 Analysis of system errors caused by wavelength index uncertainty

The signals at 299 nm is used to retrieve the aerosol backscattering coefficient and extinction coefficient due to the ozone absorption at this wavelength being negligible. In addition, the signals at 299 nm are also used to obtain real-time correction terms for aerosol extinction and backscattering. Figure 8 shows the time series of the vertical profiles of the aerosol extinction coefficient at 299 nm obtained by the ozone lidar between 26 October and 3 November 2018 at a time resolution of 12 min. During the observation period, the boundary layer height had an obvious diurnal variation pattern before 30 October. The boundary layer height was about 2 km, and the aerosol extinction coefficient was lower than 0.3 km^{-1} . The boundary layer height decreased from 31 October to 3 November, during which the maximum boundary layer height was about 1.4 km. Meanwhile, the concentration of particulate matter in the boundary layer increased significantly, and the maximum aerosol extinction coefficient was 1.2 km^{-1} . From 31 October to 1 November, the downward transport of aerosols occurred within the height range of 1.4 to 2 km. During the observation period, the aerosols in the boundary layer and free troposphere had distinct distribution patterns with relatively higher concentration levels of about 0.3 to 1 km^{-1} in the boundary layer. The vertical observations of the aerosol extinction coefficient could also effectively capture the transport of aerosol in the lower free troposphere, as shown in Fig. 8. In addition, the aerosol observations could be used to study the influence of the spatial variations and aerosol concentration levels on the uncertainty of ozone retrieval.

The aerosol correction term ($E_a + B$) was shown in Fig. 9. Values of the aerosol correction were small when the aerosol extinction coefficient was lower than 0.5 km^{-1} before 30 October. However, when the aerosol concentration sharply increased and strongly varied (such as from 31 October to 3 November), particularly on the boundary layer top and during the aerosol transport process, the aerosol correction term also increased suddenly, often exceeding 15 ppb, which cannot be ignored.

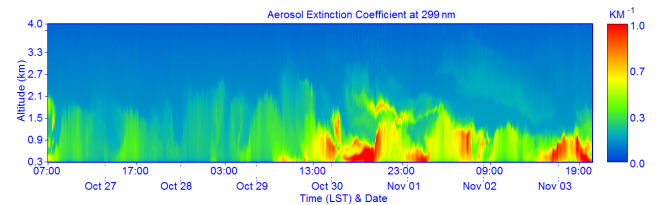


Figure 8. Time series plot of the aerosol extinction coefficient at 299 nm from the ozone lidar between 26 October and 3 November 2018 at a 12 min temporal resolution.

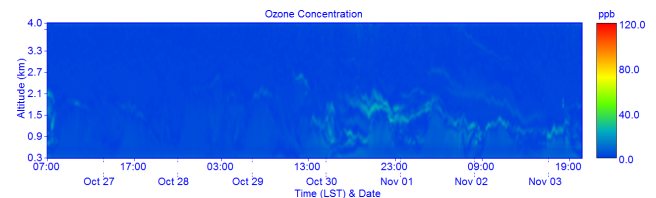


Figure 9. Time series of the vertical profiles of the aerosol correction term ($E_a + B$) between 26 October and 3 November 2018.

Figure 10a shows the aerosol correction term ($E_a + B$) obtained at 300, 500, 1500 and 2000 m from 26 October to 3 November 2018. The 300 m height is basically within the boundary layer, and the aerosol correction term fluctuated around 10 ppb. Before 30 October, the aerosol correction terms were below 5 ppb at altitudes of 500, 1000, 1500 and 2000 m. From 30 October to 3 November, when the aerosol concentration in the boundary layer was high and the aerosol transportation was found outside the boundary layer from 1.4 to 1.8 km, the aerosol correction terms changed dramatically, which was consistent with the boundary layer characteristics. The maximum value of the aerosol correction term reached about 20 ppb. The vertical distribution characteristics of aerosol correction terms were analyzed at typical sampling periods. As shown in Fig. 10b, at 18:00 LST on 27 October and 17:58 LST on 29 October 2018, the aerosol concentrations were relatively low, and the aerosol correction terms decreased with the increase in height between 0.3 and 3.5 km. The aerosol correction terms were about 10 ppb at 300 m. Above 500 m, it rapidly dropped to below 4 ppb and became smaller with the increase in height, which had little influence on the retrieval of ozone. At 17:58 LST on 31 October, the vertical profile of the aerosol correction term also changed dramatically between 1.5 and 2.2 km, resulting in a bimodal distribution pattern. In the boundary layer where the aerosol concentration was high, the aerosol correction term also exhibited a bimodal distribution pattern with dramatic changes from the lowest level of 4 to 14 ppb. The analysis indicates that the aerosol correction term exhibits rapid fluctuations during the transport of aerosols, particularly when the concentration of boundary layer aerosols is elevated. Therefore, it is necessary to correct the ozone retrieval results in real time using the aerosol correction term.

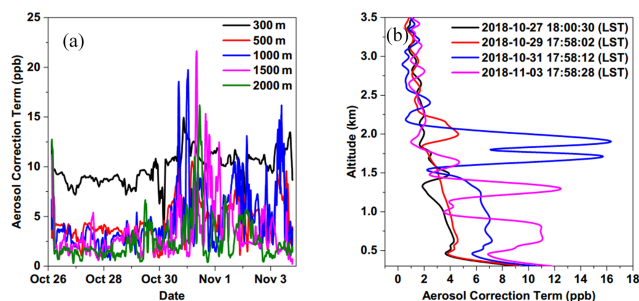


Figure 10. Aerosol correction terms at different heights and times between 26 October and 3 November 2018.

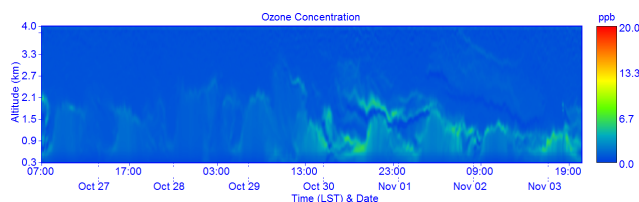


Figure 11. Aerosol correction term errors when k and μ are changed from 1 to 0.

Figure 11 shows the errors in aerosol correction terms caused by changes in k and μ from 1 to 0.6. From Eq. (2) it can be seen that when the variation in k and μ of both was 0.4, the resulting aerosol correction term errors were basically the same, and the maximum aerosol correction term errors caused by dramatic changes in aerosol were about 5 ppb. Figure 12 shows the aerosol correction term errors of k and μ from 1 to 1.4 at different heights and times. Before 30 October, the errors of the aerosol correction term in the range of 300 m–3.5 km were all less than 2 ppb. At 17:58 LST on 31 October 2018, the maximum error of aerosol correction term was 5 ppb during aerosol transport between 1.5 and 2.2 km; the error showed a single-peak distribution pattern. The aerosol correction error is acceptable for ozone monitoring and meets the detection requirements to study the characteristics of ozone diurnal variations and the upper-ozone transport.

5 Field validation with vertical observations of a tethered balloon

The developed ozone lidar was deployed in a field campaign that was conducted to make vertical observations of air pollutants using a large tethered balloon platform. The campaign was carried out in December 2018 in the city of Baoding, Wangdu County, Hebei Province, China, which is located in the center of the Beijing–Tianjin–Shijiazhuang economic triangle shown in Fig. 13a. It is a typical site for studying air pollution in the Beijing–Tianjin–Hebei region. The tethered balloon is equipped with a high-performance mini air sta-

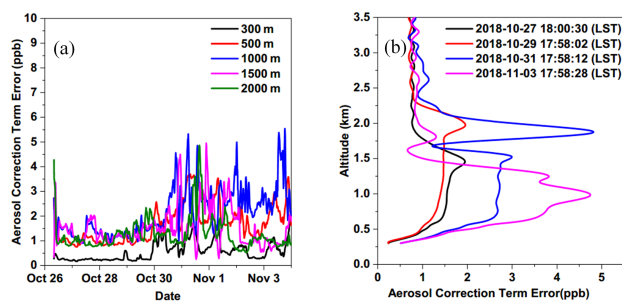


Figure 12. Aerosol correction term errors when k and μ are changed from 1 to 1.4 at different heights and times.



Figure 13. (a) Field campaign in Wangdu County during December 2018. (b) MAS-AF300 air quality monitoring system.

tion (MAS-AF300 Sapiens, Hong Kong) (Sun et al., 2016) which can measure up to six gaseous pollutants simultaneously, including O₃ concentration at different heights from where the tethered balloon was launched. It shows reliable performance under the wide range of environmental conditions, which warrants its application in the vertical measurement of ozone concentration under fast-changing meteorological conditions. Figure 13b shows the instrument.

During the campaign, an O₃ analyzer (model 49i, Thermo Fisher Scientific Inc., USA) was used for ground-level observations. Figure 14 shows the measurement result comparisons of MAS-AF300 and model 49i O₃ analyzer at 5 min resolution during 15 to 16 December before the field experiments. MAS-AF300 showed strong correlation to model 49i ($R^2 > 0.9$). The average concentration differences found were 2.3 ppb based on error analysis results. The comparison results indicated that the sensor could be accepted as a reference data source to evaluate the O₃ lidar performance.

Figure 15 presents the observations of the O₃ lidar from 19 to 22 December. The vertical resolution is 100 m, and the temporal resolution is 700 s. Ozone concentrations were on average 34.8 ppb in the range of 0.3 to 2 km. The ozone concentrations observed below 700 m exhibit a significant diurnal variation pattern with high values occurring in the afternoon period. The ozone peak value at 300 m on 20 and 21 December is 49 and 54 ppb, respectively. However, the ozone concentration rose to 46 ppb at 03:46 LST on 21 December, corresponding to 23 ppb at 19:21 LST on 20 December. As

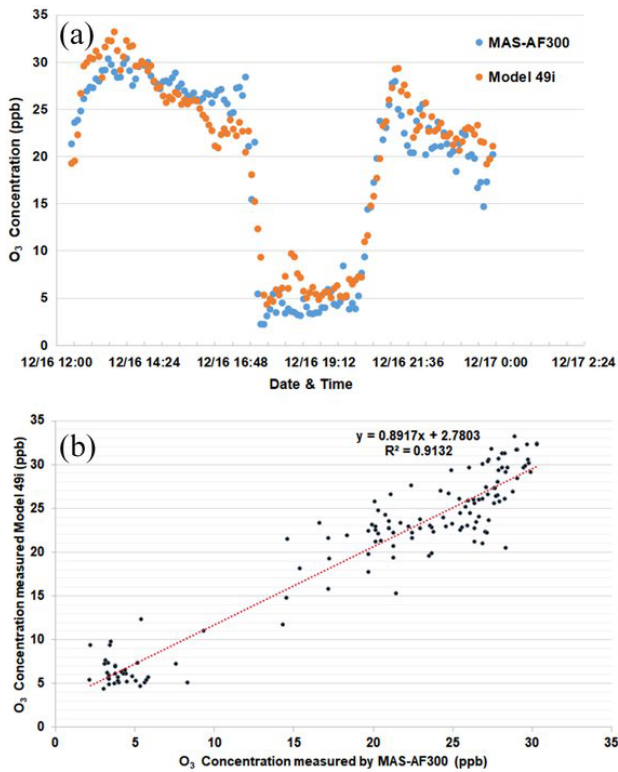


Figure 14. Comparison of the O₃ concentration from MAS-AF300 and model 49i: (a) time series plot and (b) correlation between MAS-AF300 and model 49i.

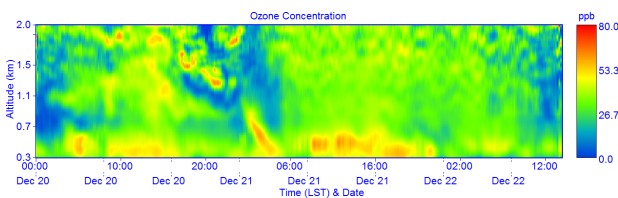


Figure 15. Time series plot of O₃ concentrations at different heights measured by O₃ lidar.

shown in Fig. 15, ozone concentrations in the height range of 700–1000 m are rapidly mixed down to a height of 300 m, resulting in a sudden increase in ozone concentration at night.

The vertical profiles of ozone were obtained when the balloon was controlled to ascend or descend, and the pollutant at a fixed height could be studied when the balloon was hovering. The maximum operating height of the tethered balloon is 900 m, while the lowest detection height of the ozone lidar is about 300 m, so the profiles measured by the two instruments ranging from 300 to 900 m are mainly compared. While the ozone concentration profiles measured by ozone lidar are the cumulative averages of 400 s worth of data, the temporal resolution of the ozone data measured by MAS-AF300 is 1 min. The balloon recorded ozone data during a landing that took 25 to 30 min. The vertical resolution of the

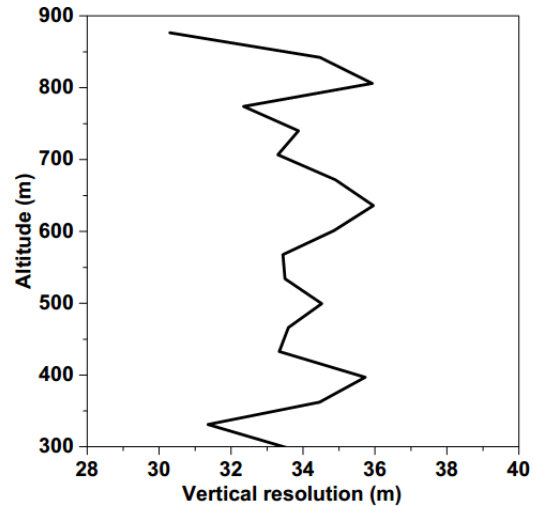


Figure 16. The vertical resolution of ozone data measured by a captive balloon.

ozone data recorded by the balloon varied with the rise rate of the tethered balloon, as shown in Fig. 16. The average of the vertical resolution is 33.7 m. Figure 17 shows comparisons of the O₃ concentration from ozone lidar measurements and tethered balloon for vertical profiles determined at different times periods on 20 December and for the time segments of ozone concentration at fixed heights of 400 and 500 m. In general, the lidar results are very consistent with the tethered balloon observations. The relative difference is 5 ppb within most altitude ranges and at most times at fixed heights of 400 and 500 m, so possible reasons for the difference may be caused by the different vertical resolution and temporal resolution of the lidar and the tethered balloon. In particular, as shown in Fig. 15, the ozone air mass within 800–1000 m was transported almost to the near ground, which was confirmed by the tethered balloon at 500 m, as shown in Fig. 17d. As can be seen in this figure, under the influence of the descending ozone air mass, the ozone concentration observed by both the ozone lidar and the tethered balloon increased from 35 ppb at 00:00 LST to approximately 50 ppb at 03:00 LST at 500 m, which then gradually fell.

6 Conclusions

In this paper, a differential absorption lidar for the simultaneous observations of lower-tropospheric ozone is described in detail, which was based on a single CO₂ Raman cell and the high-resolution grating spectrometer. A flashlamp-pumped Nd:YAG laser, which provides 90 mJ output at a wavelength of 266 nm and a 10 Hz pulse repetition rate, is used as the pump source for the CO₂ Raman cell. The CO₂ Raman cell is filled with 16 bar (1.6 MPa) pure CO₂ at 99.999 % purity. The laser energy outputs of 276, 287 and 299 nm are 8.4, 7.7 and 4.2 mJ, respectively. A 250 mm telescope and the grating

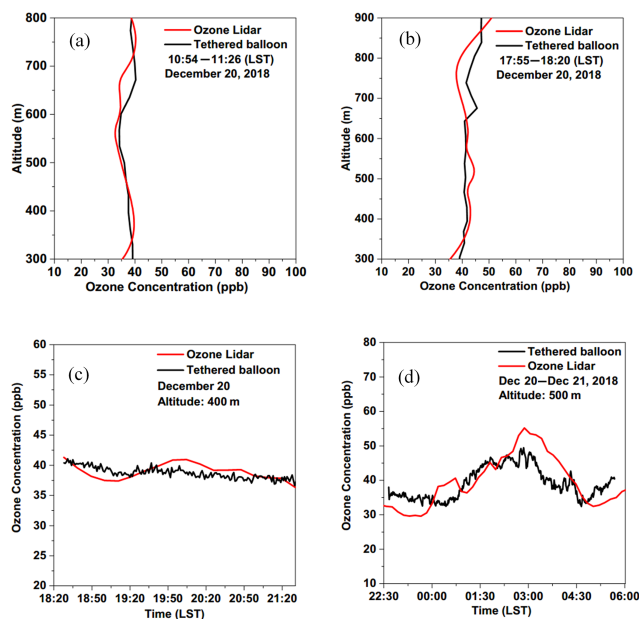


Figure 17. Comparison of the O₃ concentrations from the tethered balloon and O₃ lidar measurements for vertical profiles determined at different times on 20 December and at fixed heights of 400 and 500 m.

spectrometer compose the lidar receiver. For signal acquisition, in order to reduce the influence of the A/D electronic noise on the atmospheric echo signal, amplifiers of 2 times and 48 times are adopted for the same echo signal, respectively for the near-altitude signal and the long-altitude signal. Within the range of 500 m–1 km, the echo signals of 2-times magnification and 48-times magnification are fused using the least-squares method.

Take SF and SNR into account: below 600 m, the signals at the wavelengths of 276 and 287 nm were used to retrieve the ozone concentration profile; above 600 m, the signals at 287 and 299 nm were used. The statistical error from 200 to 600 m gradually increased from 2.35 % to 6.9 %. The statistical error of ozone from 600 m to 2.7 km was basically within 3 %. From 2.7 to 3.9 km, the statistical error gradually increased to about 18 %. We also evaluated the errors caused by wavelength index uncertainty. Some examples at different aerosol distributions and concentrations at Hefei are provided to illustrate the errors caused by Angstrom wavelength index uncertainty, while the results, ranging from 0.6 to 1.4, revealed that the maximum error of the aerosol correction term was 5 ppb; the error displayed a single-peak distribution.

The developed ozone lidar was deployed in a field experiment conducted with vertical profile observations using a tethered balloon. The observed lidar ozone results exhibited good agreement with those observed by the tethered balloon, confirming that the ozone lidar measurements are accurate. The blind zone of the ozone lidar is about 300 m. In future work, we plan to design a 100 mm telescope to extend

the observation range starting from the near surface (about 100 m) and study the exchange between near-surface and tropospheric ozone.

Data availability. Lidar measurements are available upon request.

Author contributions. GF developed the methodology, designed the ozone lidar, developed the analysis code and wrote the manuscript. YF developed the A/D data acquisition system. JH contributed to data analysis. YX performed lidar measurements. TZ and WL participated in methodology development and supervised the project. ZN supported the ozone data of MAS-AF300.

Competing interests. The contact author has declared that none of the authors has any competing interests.

Disclaimer. Publisher's note: Copernicus Publications remains neutral with regard to jurisdictional claims made in the text, published maps, institutional affiliations, or any other geographical representation in this paper. While Copernicus Publications makes every effort to include appropriate place names, the final responsibility lies with the authors.

Acknowledgements. This research has been supported by the National Key Research and Development Program of China (grant no. 2022YFC3700400), Hefei Comprehensive National Science Center, and the National Natural Science Foundation of China (grant nos. 42005106, 41941011).

Financial support. This research has been supported by the National Key Research and Development Program of China (grant no. 2022YFC3700400) and the National Natural Science Foundation of China (grant nos. 42005106 and 41941011).

Review statement. This paper was edited by Bin Yuan and reviewed by two anonymous referees.

References

- Browell, E. V., Ismail, S., and Grant, W. B.: Differential absorption lidar (DIAL) measurements from air and space, *Appl. Phys. B*, 67, 399–410, <https://doi.org/10.1007/s003400050523>, 1998.
- Chen, X., Zhong, B. Q., Huang, F. X., Wang, X. M., Sarkar, S., Jia, S. G., Deng, X. J., Chen, D. H., and Shao, M.: The role of natural factors in constraining long-term tropospheric ozone trends over Southern China, *Atmos. Environ.*, 220, 117060, <https://doi.org/10.1016/j.atmosenv.2019.117060>, 2020.
- Chi, X., Liu, C., Xie, Z., Fan, G., Wang, Y., He, P., Fan, S., Hong, Q., Wang, Z., Yu, X., Yue, F., Duan, J., Zhang, P., and Liu, J.: Observations of ozone vertical profiles and corresponding precursors

- in the low troposphere in Beijing, China, *Atmos. Res.*, 213, 224–235, <https://doi.org/10.1016/j.atmosres.2018.06.012>, 2018.
- Clain, G., Baray, J. L., Delmas, R., Keckhut, P., and Cammas, J. P.: A lagrangian approach to analyse the tropospheric ozone climatology in the tropics: Climatology of stratosphere-troposphere exchange at Reunion Island, *Atmos. Environ.*, 44, 968–975, <https://doi.org/10.1016/j.atmosenv.2009.08.048>, 2010.
- Dolgii, S. I., Nevzorov, A. A., Nevzorov, A. V., Romanovskii, O. A., and Kharchenko, O. V.: Intercomparison of Ozone Vertical Profile Measurements by Differential Absorption Lidar and IASI/MetOp Satellite in the Upper Troposphere-Lower Stratosphere, *Remote Sens.*, 9, 447, <https://doi.org/10.3390/rs9050447>, 2017.
- Fan, G., Zhang, B., Zhang, T., Fu, Y., Pei, C., Lou, S., Li, X., Chen, Z., and Liu, W.: Accuracy of evaluation of differential absorption lidar for ozone detection and intercomparisons with other instruments, *Remote Sens.*, 16, 2369, <https://doi.org/10.3390/rs16132369>, 2024.
- Fix, A., Wirth, M., Meister, A., Ehret, G., Pesch, M., and Weidauer, D.: Tunable ultraviolet optical parametric oscillator for differential absorption lidar measurements of tropospheric ozone, *Appl. Phys. B*, 75, 153–163, <https://doi.org/10.1007/s00340-002-0964-y>, 2002.
- Hwang, I. D., Veselovsky, I. A., Lee, C. H., and Lee, Y. W.: Raman Conversion of Krf Laser in Mixed H₂+D₂ Gas and D₂ for Tropospheric Ozone Sounding, *IEEE Leos. Ann. Mtg., LEOS'93*, 736–737, <https://doi.org/10.1109/LEOS.1993.379401>, 1993.
- Koo, B., Jung, J., Pollack, A. K., Lindhjem, C., Jimenez, M., and Yarwood, G.: Impact of meteorology and anthropogenic emissions on the local and regional ozone weekend effect in Midwestern US, *Atmos. Environ.*, 57, 13–21, <https://doi.org/10.1016/j.atmosenv.2012.04.043>, 2012.
- Kuang, S., Newchurch, M. J., Burris, J., and Liu, X.: Ground-based lidar for atmospheric boundary layer ozone measurements, *Appl. Opt.*, 52, 3557–3566, <https://doi.org/10.1364/AO.52.003557>, 2013.
- Langford, A. O., Alvarez II, R. J., Kirgis, G., Senff, C. J., Caputi, D., Conley, S. A., Faloon, I. C., Iraci, L. T., Marrero, J. E., McNamara, M. E., Ryoo, J.-M., and Yates, E. L.: Intercomparison of lidar, aircraft, and surface ozone measurements in the San Joaquin Valley during the California Baseline Ozone Transport Study (CABOTS), *Atmos. Meas. Tech.*, 12, 1889–1904, <https://doi.org/10.5194/amt-12-1889-2019>, 2019.
- Li, X. B., Wang, D. F., Lu, Q. C., Peng, Z. R., Fu, Q. Y., Hu, X. M., Huo, J. T., Xiu, G. L., Li, B., Li, C., Wang, D. S., and Wang, H. Y.: Three-dimensional analysis of ozone and PM_{2.5} distributions obtained by observations of tethered balloon and unmanned aerial vehicle in Shanghai, China, *Stoch. Env. Res. Risk A*, 32, 1189–1203, <https://doi.org/10.1007/s00477-018-1524-2>, 2018.
- Lokoshchenko, M. A. and Shifrin, D. M.: Temperature stratification and altitude ozone variability in the low troposphere from acoustic and balloon sounding, *Russ. Meteorol. Hydrol.*, 34, 72–82, <https://doi.org/10.3103/S1068373909020022>, 2009.
- Machol, J. L., Marchbanks, R. D., Senff, C. J., McCarty, B. J., Eberhard, W. L., Brewer, W. A., Richter, R. A., Alvarez, R. J., Law, D. C., Weickmann, A. M., and Sandberg, S. P.: Scanning tropospheric ozone and aerosol lidar with double-gated photomultipliers, *Appl. Opt.*, 48, 512–524, <https://doi.org/10.1364/AO.48.000512>, 2009.
- Nakazato, M., Nagai, T., Sakai, T., and Hirose, Y.: Tropospheric ozone differential-absorption lidar using stimulated Raman scattering in carbon dioxide, *Appl. Opt.*, 46, 2269–2279, <https://doi.org/10.1364/AO.46.002269>, 2007.
- Olsen, M. A., Schoeberl, M. R., and Douglass, A. R.: Stratosphere-troposphere exchange of mass and ozone, *J. Geophys. Res.-Atmos.*, 109, D24, <https://doi.org/10.1029/2004JD005186>, 2004.
- Osterman, G. B., Kulawik, S. S., Worden, H. M., Richards, N. A. D., Fisher, B. M., Eldering, A., Shephard, M. W., Froidevaux, L., Labow, G., Luo, M., Herman, R. L., Bowman, K. W., and Thompson, A. M.: Validation of Tropospheric Emission Spectrometer (TES) measurements of the total, stratospheric, and tropospheric column abundance of ozone, *J. Geophys. Res.-Atmos.*, 113, D15, <https://doi.org/10.1029/2007JD008801>, 2008.
- Qian, Y., Luo, Y., Si, F., Zhou, H., Yang, T., Yang, D., and Xi, L.: Total ozone columns from the environmental trace gases monitoring instrument (EMI) using the DOAS method, *Remote Sens.*, 13, 2098, <https://doi.org/10.3390/rs13112098>, 2021.
- Schuepbach, E., Davies, T. D., Massacand, A. C., and Wernli, H.: Mesoscale modelling of vertical atmospheric transport in the Alps associated with the advection of a tropopause fold – a winter ozone episode, *Atmos. Environ.*, 33, 3613–3626, [https://doi.org/10.1016/S1352-2310\(99\)00103-X](https://doi.org/10.1016/S1352-2310(99)00103-X), 1999.
- Sullivan, J. T., McGee, T. J., Sumnicht, G. K., Twigg, L. W., and Hoff, R. M.: A mobile differential absorption lidar to measure sub-hourly fluctuation of tropospheric ozone profiles in the Baltimore–Washington, D.C. region, *Atmos. Meas. Tech.*, 7, 3529–3548, <https://doi.org/10.5194/amt-7-3529-2014>, 2014.
- Sun, L., Wong, K. C., Wei, P., Ye, S., Huang, H., Yang, F. H., Westerdahl, D., Louie, P. K. K., Luk, C. W. Y., and Ning, Z.: Development and Application of a Next Generation Air Sensor Network for the Hong Kong Marathon 2015 Air Quality Monitoring, *Sensors-Basel*, 16, 211, <https://doi.org/10.3390/s16020211>, 2016.
- Wang, M. and Fu, Q.: Changes in stratosphere-troposphere exchange of air mass and ozone concentration in CCM1 models from 1960 to 2099, *J. Geophys. Res.-Atmos.*, 128, <https://doi.org/10.1029/2023JD038487>, 2023.
- Wang, T., Xue, L. K., Brimblecombe, P., Lam, Y. F., Li, L., and Zhang, L.: Ozone pollution in China: A review of concentrations, meteorological influences, chemical precursors, and effects, *Sci. Total Environ.*, 575, 1582–1596, <https://doi.org/10.1016/j.scitotenv.2016.10.081>, 2017.
- Wang, X., Xiang, Y., Liu, W., Lv, L., Dong, Y., Fan, G., Ou, J., and Zhang, T.: Vertical profiles and regional transport of ozone and aerosols in the Yangtze River Delta during the 2016 G20 summit based on multiple lidars, *Atmos. Environ.*, 259, 118506, <https://doi.org/10.1016/j.atmosenv.2021.118506>, 2021.
- Worden, H. M., Logan, J. A., Worden, J. R., Beer, R., Bowman, K., Clough, S. A., Eldering, A., Fisher, B. M., Gunson, M. R., Herman, R. L., Kulawik, S. S., Lampel, M. C., Luo, M., Megretskaia, I. A., Osterman, G. B., and Shephard, M. W.: Comparisons of Tropospheric Emission Spectrometer (TES) ozone profiles to ozonesondes: Methods and initial results, *J. Geophys. Res.-Atmos.*, 112, D3, <https://doi.org/10.1029/2006JD007258>, 2007.